Catalysis Today 165 (2011) 49–55

Contents lists available at ScienceDirect

Catalysis Today

journal homepage: www.elsevier.com/locate/cattod

Adsorption and reactions of NO_x on RuO_2(1 1 0)

Hangyao Wang[a,1], William F. Schneider[a,b,*]

[a] Department of Chemical and Biomolecular Engineering, University of Notre Dame, Notre Dame, IN 46556, USA
[b] Department of Chemistry and Biochemistry, University of Notre Dame, Notre Dame, IN 46556, USA

ARTICLE INFO

Article history:
Received 1 October 2010
Received in revised form
15 November 2010
Accepted 16 November 2010
Available online 17 December 2010

Keywords:
NOx
Metal oxides
DFT
Ruthenium oxide
NO oxidation
NO decomposition

ABSTRACT

The surface chemistry of NO_x on metal oxides is important to environmental catalysis. Here we employ plane-wave, supercell DFT calculations to characterize NO_x chemistry at the RuO_2(1 1 0) surface as a model of a catalytically active transition metal oxide surface. We identify a range of potential NO_x intermediates, and use a thermodynamic analysis to characterize their stability as a function of gas exposure conditions. Adsorbed NO (nitrosyl) and to a lesser extent NO_3 (nitrate) dominate the surface phase diagram. Computed vibrational spectra are in good agreement with observation and provide new assignments of observed surface species. NO_2 is thermodynamically unstable at the surface and its desorption is never favored: in contrast to its activity towards CO oxidation, RuO_2(1 1 0) is not an effective NO oxidation catalyst. Rather, it could be effective as a reversible NO adsorber. Finally, we characterize the kinetics of several NO surface reactions and identify a pathway that may contribute to the decomposition of NO to N_2 and N_2O over partially reduced surfaces.

1. Introduction

The oxides of nitrogen (NO_x) are common air pollutants that contribute to the formation of acid rain and photochemical smog, in addition to being health hazards themselves. For this reason, the catalytic chemistry of NO_x is of considerable practical interest [1,2]. The most elementary of NO_x reactions is the catalytic oxidation of NO to NO_2:

$$NO + \frac{1}{2}O_2 \rightarrow NO_2 \quad (1)$$

Pt is the most common NO oxidation catalysis, but Pt suffers deactivating oxidation under typical NO oxidation conditions [3]. There is considerable interest in identifying alternative catalysts, in particular metal oxides that might be less expensive and more robust catalytic materials [4]. Further, metal oxides are the active component of so-called "NO_x traps", which are used to temporarily store NO_x as nitrates (NO_3^-) [5]. This competition between oxidation and storage makes the surface chemistry of NO_x on metal oxides particularly interesting.

The (1 1 0) surface of RuO_2 has received a considerable amount of attention as a model for study catalytic chemistry at an oxide surface, in particular with respect to its activity for catalytic CO oxidation [6–15]. Recently we described the competing formation of surface carbonate and bicarbonate that can poison the CO oxidation activity [16,17]. Less thoroughly studied is the NO_x chemistry of RuO_2 [18–21]. Thermal desorption spectroscopy (TDS) and high resolution electron energy loss spectroscopy (HREELS) show that NO interacts with surface oxygen to produce surface NO_2 species, and that these desorb as NO without the production of gas-phase NO_2 [18,20]. Rather than NO_2, small amounts of N_2O and N_2 are observed to form during low-temperature NO dosing experiments [18]. The CO and NO oxidation chemistries are thus quite different, a distinction that has been ascribed to the relatively higher adsorption energy of NO at the (1 1 0) surface [19]. Dimers of NO have been proposed as precursors to N_2O [19], but the pathways to N_2 are unknown. Higher oxides of nitrogen, in particular nitrate-like NO_3 species, have not been reported on RuO_2.

Bulk rutile RuO_2 is comprised of 6-fold coordinated Ru^{4+} cations and 3-fold coordinated O^{2-} anions. The stoichiometric (1 1 0) surface (Fig. 1) exposes rows of 2-fold bridging (O_{br}) and 3-fold (O_{3f}) oxygen as well as 5-fold coordinated, or "coordinatively unsaturated" and partially reduced, Ru_{cus}. O_{br} vacancies expose 4-fold Ru centers, and excess oxygen can be accommodated at the cus sites, i.e., O_{cus} [22]. Coupled with the ability of the NO_x species to behave as electron acceptors or donors at oxide surfaces [23], one can anticipate a rich RuO_2–NO_x surface chemistry. In this work, we use plane-wave, supercell density functional theory (DFT) models to characterize potential NO_x (x = 1,2,3) intermediates at RuO_2(1 1 0) as a function of surface state and adsorbate coverage. The results are useful in explaining surface species identified spectroscopically in

* Corresponding author. Tel.: +1 574 631 8754; fax: +1 574 631 8366.
E-mail address: wschneider@nd.edu (W.F. Schneider).
[1] Present address: Department of Chemical Engineering, University of Delaware, Newark, DE 19716, USA.

0920-5861/$ – see front matter © 2010 Elsevier B.V. All rights reserved.
doi:10.1016/j.cattod.2010.11.046

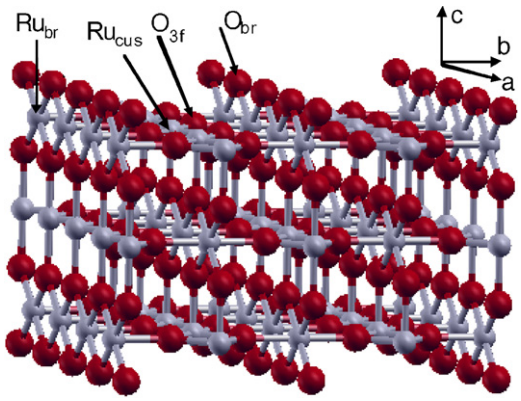

Fig. 1. Ball and stick representation of RuO_2(1 1 0) surface with red balls representing oxygen and grey balls ruthenium. The directions *a*, *b* and *c* are [0 0 1], [$\bar{1}$ 1 0] and [110], respectively. The definitions of O_{br}, O_{3f} and Ru_{cus} are indicated in the figure. (For interpretation of the references to color in this figure legend, the reader is referred to the web version of the article.)

a number of experiments. A thermodynamic free energy analysis is used to compare the stability of these as a function of external gas conditions. Interestingly, cus-bound NO is found to be the most stable surface species over a wide range of conditions; oxidized NO_x is predicted to exist primarily as surface-bound nitrate, or NO_3. The reaction barriers of oxidation and dissociation reactions of adsorbed NO are calculated and contrasted. RuO_2 is found not to be an effective NO oxidation catalyst, but it is effective in adsorbing and potentially in decomposing NO.

2. Computational details

Periodic supercell, plane wave density functional theory (DFT) calculations were performed using version 4.6.26 of the Vienna ab Initio Simulation Package (VASP) [24]. Core–valence electron interactions are treated within the projector augmented wave (PAW) approximation [25,26]. Electronic energies and forces were calculated within the non-spin-polarized generalized gradient approximation (GGA) using the PW91 functional. Test calculations show that spin-polarization introduces a nearly constant shift in total energy that cancels out in binding energy calculations; all reported surface energies are non-spin-polarized. Isolated NO, NO_2, and NO_3 are odd-electron, paramagnetic species and are calculated spin-polarized in a $15 \times 15 \times 15$ Å supercell.

Most surface calculations are performed within a tetragonal 3×1 surface supercell, which includes three Ru_{cus} ions and has lateral dimensions $a = 9.4161$ and $b = 6.4284$ Å. A $6 \times 8 \times 1$ Monkhorst-Pack mesh is used to sample the first Brillouin zone (12 symmetry-unique *k*-points). A cutoff energy of 400 eV is used for the plane waves. More computational details can be found in previous publications [16,22,27]. These parameters were sufficient to converge calculated energies to <0.01 eV and gradients to at least <0.03 eV/Å.

Vibrational frequencies are obtained by diagonalization of the Hessian matrix, calculated by displacing atoms of interest by 0.01 Å from their equilibrium positions while fixing other atoms. Minimum energy reaction paths (MEPs) were calculated using the Climbing Image Nudged Elastic Band (CI-NEB) method [28,29]. In this method, a chain of images spanning the reaction coordinated are connected by springs and relaxed simultaneously to the MEP. The CI-NEB method modifies the original NEB method [30,31] by forcing one intermediate image to a saddle point, where the molecular forces vanish. Vibrational frequency analysis confirms that the reported saddle points have a single imaginary vibrational mode and are transition states. The reaction barriers are obtained by subtracting the energy at the transition state from that at the initial state. A Bader partitioning of charge densities is used to assign net atomic and molecular charges [32,33].

3. Results

3.1. NO adsorption

We first consider NO adsorbed at two types of exposed Ru surface sites. Removal of an O_{br} from the stoichiometric (1 1 0) surface exposes undercoordinated Ru sites that can accommodate CO [34] and O_2 [27]. Similarly, we find NO to bind in at least four distinct binding modes at this bridge vacancy, shown in Fig. 2a–d. Relevant bond distances are indicated in this figure, and Table 1 summaries calculated N–O stretching frequencies. Most preferred is adsorp-

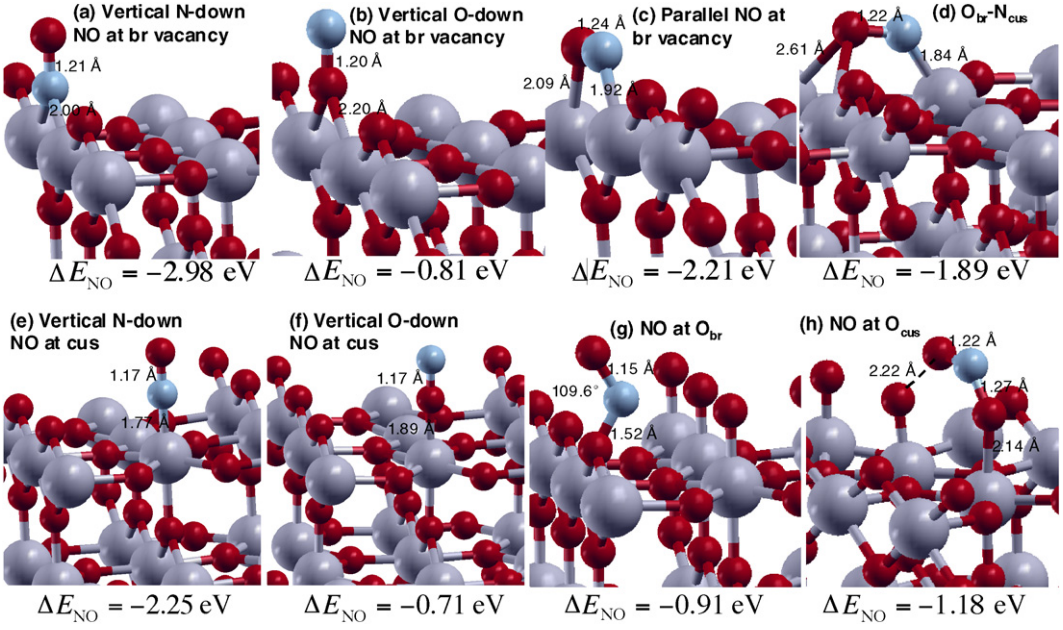

Fig. 2. Calculated NO adsorption configurations at the RuO_2(1 1 0) surface.

Table 1
Key computed harmonic and (as available, in parenthesis) experimental [20] vibrational energies of adsorbed NO_x.

	Structure	Frequency (meV)	Structure	Frequency (meV)
NO atop Ru	2(a)	197.5 (193)	2(b)	190.5
	2(c)	166.9	2(d)	178.5
	2(e)	231.1 (232, 230.5)	2(f)	220.6
NO_2	2(g)	161.5, 122.1, 78.6	2(h)	178.3, 130.4, 89.3
	3(a)	141.6, 136.8, 94.0	3(b)	191.2, 114.4, 92.9
	3(c)	180.2, 158.3, 94.8	3(d)	177.2, 125.3, 91.0
NO_3	3(e)	194.3 (204), 136.0, 99.1	3(f)	189.7, 126.7, 118.7
	3(g)	190.5, 149.7, 88.5		
N_2O	3(h)	290.7 (283), 161.5, 66.8		

tion N-down and upright (Fig. 2a), which occurs with an adsorption energy of nearly −3 eV, or 1 eV more exothermic than CO binding in the same location [34]. NO has low lying $2\pi^*$ states that make it a strong π acceptor, and Bader analysis indicates 0.62 $|e|$ electrons are transferred to NO in this binding mode. Consistent with this, the N–O bond length is increased 0.06 Å over its gas-phase value of 1.15 Å, and the N–O vibrational frequency of 197.5 meV (1593 cm^{-1}) is 40 meV red-shifted with respect to gas-phase NO. This adsorption configuration is likely responsible for the the weak and unassigned vibrational mode at 193 meV observed in HREELS experiments [18].

A number of other NO adsorption configurations are also possible at the bridge vacancy. O-down, vertical adsorption (Fig. 2b) is 2.2 eV less favorable than N-down adsorption and is unlikely to be important. Much lower in energy is a side-bound, bridging mode (Fig. 2c) similar to that identified for O_2 [27]. While the side-bound peroxo is preferred by about 0.6 eV over a vertically bound O_2, the opposite is true for NO. Like O_2, the N–O bond is lengthened considerably, consistent with the 0.43 $|e|$ charge transfer from reduced Ru to NO. Lastly, we find a binding mode in which NO bridges adjacent br and cus vacancies (Fig. 2d), again in analogy with O_2 [27]. The N center prefers the cus site; binding at the br site recovers vertically bound NO.

Ru_{cus} provide a second potential NO adsorption site. On a stoichiometric surface model, NO adsorbs on Ru_{cus} with bond perpendicular to the surface and N-down (Fig. 2e) or O-down (Fig. 2f). The former is preferred, with binding energies of −2.25 eV at 1/3 monolayer (ML) and −2.10 eV at full coverage (1 ML). The calculated NO adsorption energy is in good agreement with the value of −1.98 eV assigned to cus-bound NO in temperature-programmed desorption (TPD) experiments [35]. Previous DFT calculations report binding energies of −2.09 [21] and −1.7 eV [19]. The present results favor the former value. The N–O bond length is only slightly increased over the gas-phase. The linear adsorption geometry indicates significant σ donation to Ru_{cus} and π backbonding from undercoordinated and reduced Ru_{cus} into the NO $2\pi^*$ state [19]. Bader analysis is consistent with this picture, and indicates a net of 0.94 $|e|$ electron transfer to adsorbed NO. The computed N–O vibrational frequency (231 meV, or 1864 cm^{-1}, Table 1) is in excellent agreement with that assigned to Ru_{cus}-bound NO in HREELS experiments [20]. Linear and O-down NO is less effective at σ and π bonding, accepts only 0.22 $|e|$, and is 1.5 eV less stable. At a single Ru_{cus} site, then, diatomic adsorption energies decrease from NO (−2.2 eV) to CO (−1.3) [34,16] to O_2 (−0.7), [27], in parallel primarily with their π accepting strength.

The Ru_{cus}–NO adsorption energies are based on 3×1 surface supercell and thus a coverage of 1/3 ML. NO_x species can exhibit strong cooperative adsorption at base metal oxide surfaces due to charge transfer between adsorbates [23]. To probe for this effect we calculated NO adsorption energies at the most stable cus sites at various NO and O coverages. The results are as summarized in Table 2. No evidence of cooperative adsorption is found here. Rather, adsorbate–adsorbate interactions are weakly repulsive.

Table 2
NO adsorption energies at cus sites in a 3×1 cell at different adsorbate coverages.

Site	Occupancy	NO coverage (ML)	ΔE_{NO} (eV)
cus	NO, –, –	1/3	−2.25
cus	NO, NO, –	2/3	−2.20
cus	NO, NO, NO	1	−2.10
cus	NO, O, –	1/3	−2.22
cus	NO, O, O	1/3	−2.17
cus	NO, NO, O	2/3	−2.15

NO_{cus}–NO_{cus} interactions are approximately 0.05 eV, consistent with previous reports [19]. This lateral interaction is only half of that found for O_{cus}–O_{cus} interactions [22]. The lateral interaction energy between neighbor NO and O is even smaller, only 0.03 eV. Along the cus rows, at least, cooperative interactions are not present.

Unlike CO or O_2 and because of its particularly strong π accepting ability, NO is also able to adsorb at surface O sites in addition to surface Ru. To isolate the binding to single surface oxygen, we consider an oxygen-rich (1 1 0) surface saturated with O in both bridge and cus sites [22,27]. At O_{br} (Fig. 2g), NO binds from the side to form a bent and asymmetric NO_2 fragment. Binding is 0.27 eV stronger along the O_{cus} row (Fig. 2h) and forms a more symmetric NO_2 fragment. Calculated adsorption energies are −0.9 and −1.2 eV, respectively. This robust NO binding even at the O-saturated surface is consistent with the observed adsorption of NO on an O-saturated surface [20]. Bader charge analysis shows that the net charge on the NO adsorbate is +0.34 and +0.32 $|e|$ atop O_{br} and O_{cus}, respectively. NO atop O thus acts as a net electron donor rather than acceptor, in contrast to its role on Ru. The NO together with the surface O can be viewed approximately as a nitrite (NO_2^-), and consistent with this view, the net Bader charge on the NO_2 unit is −0.37 and −0.41 $|e|$, respectively. The slight lengthening of N–O bond lengths and decrease in NO_2 angle compared to that of gas-phase NO_2 are also consistent with a fragment that is NO_2^--like.

3.2. NO_2 adsorption

The more oxidized forms of NO_x, NO_2 and NO_3, tend to be present only under relatively strongly oxidizing conditions. We focus, then, on their Ru adsorption chemistry in the cus sites that are more likely to be available under such conditions. The bent NO_2 molecule exhibits a rich coordination chemistry in general, and consistent with this, the top half of Fig. 3 shows that NO_2 adsorbs in Ru_{cus} sites in at least four distinct conformations. In order of decreasing adsorption energy, these include O-down and bridging two Ru_{cus} (Fig. 3a), side-bound and bridging two Ru_{cus} (Fig. 3b), N-down and atop a single Ru_{cus} (Fig. 3c) and O-down and atop a single Ru_{cus} (Fig. 3d). Adsorption energies range from −1.76 to −1.24 eV, and thus are inside the range found for NO. In general, the N–O bond lengths in these adsorption configurations are slightly longer (at most 0.12 Å in Fig. 3b) than that of gas-phase NO_2. As with NO, NO_2 adsorption is accompanied by charge trans-

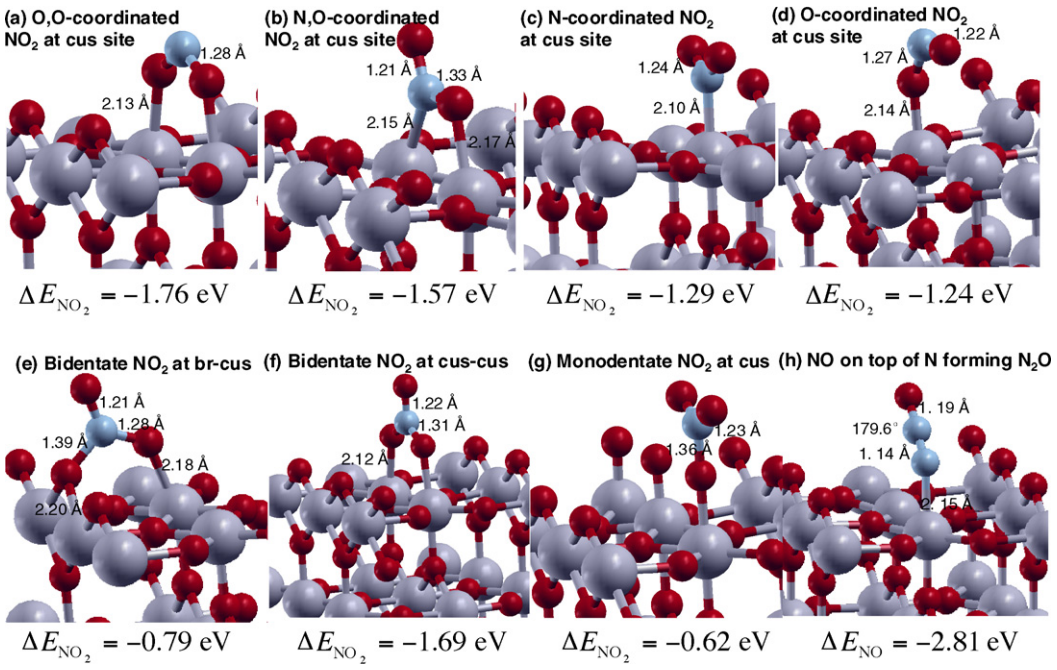

Fig. 3. Adsorption configurations and energies of NO_2 on the $RuO_2(1\,1\,0)$ surface relative to gas phase NO_2.

fer from the reduced Ru centers to NO_2. The two bidentate NO_2 modes (Fig. 3a and b) each gain around 0.52 $|e|$ charge, about 0.08 $|e|$ more than the two monodentate modes (Fig. 3c and d). The two N–O stretching and one bending vibrational frequencies are listed in Table 1.

Like NO, NO_2 can also bind at surface O sites, in this case to form planar nitrate (NO_3^-) species analogous to the carbonates formed via CO_2 adsorption [17]. At a fully O-saturated surface, NO_2 preferentially adsorbs unidentate atop an O_{cus} with binding energy of about −0.6 eV (Fig. 3g). More favorable is NO_2 binding adjacent to vacant Ru_{cus} sites, to create bidendate nitrate. Fig. 3e and f compare bidentate binding across O_{br} and Ru_{cus} and across neighbor O_{cus} and Ru_{cus}. The former leads to an asymmetric nitrate with binding energy only modestly greater than unidentate NO_2. NO_2 binding in the latter site is considerably stronger, at −1.7 eV. These adsorption energies considerably surpass the −0.55 eV binding of CO_2 to form the analogous carbonates [17]. Bader analysis shows that the NO_3 units in Fig. 3e and f carry −0.55 and −0.52 $|e|$ charge, respectively.

Fig. 4 compares the energies of adsorbed, cus-bound NO* + 2O* and its reaction products with the analogous carbon species. NO strongly adsorbs to Ru_{cus} sites and, in large part because gas-phase NO oxidation to NO_2 is only modestly exothermic, conversion of bound NO to bound NO_2 is endothermic and bound NO_3 approximately thermoneutral. Desorption of any oxidized NO_2 species is energetically costly. In contrast, CO binds substantially more weakly to Ru_{cus}, and in large measure because CO oxidation to CO_2 is quite exothermic, formation of adsorbed CO_2 or CO_3 is also quite exothermic. In contrast to the strong acid NO_2, CO_2 is relatively weakly bound at the surface and much easier to desorb. This simple picture illustrates why the expected equilibrium surface compositions and catalytic activities of RuO_2 towards NO and CO are so different. We consider the equilibrium and kinetic pictures in more detail below.

NO dosing experiments to a nearly O-saturated $RuO_2(1\,1\,0)$ surface reveal, in addition to Ru_{cus}–bound NO, two losses in HREELS at 193 and 122 meV that have been attributed to adsorbed NO_2 [20]. One interpretation of these features is as a side-bound NO_2, Fig. 3b, which we calculate to have vibrational features at 191 and 114 meV.

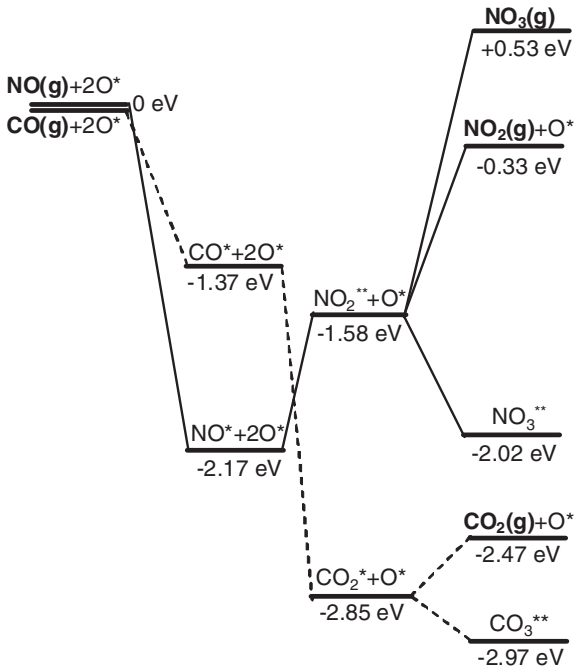

Fig. 4. Relative energies of cus-bound NO_x (solid lines) and CO_x (dashed lines) [16] on the $RuO_2(1\,1\,0)$ surface.

Based on this energy analysis, however, it is at least as likely that the observed species is a cus-row NO_3, Fig. 3f, which is energetically preferred and has computed features in the same range, at 190 and 127 meV. TDS results show that NO desorbs from this oxidized state with an energy 0.24 eV less than desorption from the cus-bound NO*. By comparison to Fig. 4, we see that loss of NO from NO* and NO_3^* are computed to differ by a similar 0.15 eV, while desorption of NO from NO_2^* is much lower in energy. While not proof, these results suggest an interpretation of observed surface NO_2 species as nitrate-like NO_3.

Table 3
Combinations of co-adsorbates (vacancy *, O^*_{cus}, NO^*_{cus}, $NO^{**}_{2,cus}$, $NO^{**}_{3,cus}$ and NO^*_{br}) used in phase diagram construction. Except the one involving NO^*_{br}, other configurations are based on stichometric surface.

Supercell	Combinations of adsorbates
2×1	*–*, O^*_{cus}–*, O^*_{cus}–O^*_{cus}, NO^*_{cus}–*, NO^*_{cus}–NO^*_{cus}, $NO^{**}_{2,cus}$, $NO^{**}_{3,cus}$, NO^*_{cus}–NO^*_{cus}/NO^*_{br}–NO^*_{br}
3×1	O^*_{cus}–O^*_{cus}–*, NO^*_{cus}–O^*_{cus}–O^*_{cus}, NO^*_{cus}–NO^*_{cus}–O^*_{cus}, $NO^{**}_{2,cus}$–*, $NO^{**}_{3,cus}$–*
4×1	O^*_{cus}–O^*_{cus}–NO^*_{cus}–*, NO^*_{cus}–O^*_{cus}–O^*_{cus}–O^*_{cus}, NO^*_{cus}–NO^*_{cus}–NO^*_{cus}–O^*_{cus}, $NO^{**}_{2,cus}$–NO^*_{cus}–*, $NO^*_{3,cus}$–NO^*_{cus}–*

3.3. Thermodynamic stability analysis of adsorbed NO_x

To determine the range of stability of these various NO_x adsorbates under real conditions in an overall oxidizing environment, we constructed a surface phase diagram as a function of NO and O_2 chemical potentials. We include in the analysis the most stable surface states of adsorbed NO (N-down on Ru_{cus}), NO_2 (O,O-bound bridging two Ru_{cus}), and NO_3 (also bridging two Ru_{cus}). To capture coverage effects, we calculated the energies of 18 combinations of these species in 2×1, 3×1 and 4×1 supercells, as depicted in Table 3.

We identify configurations with the lowest surface free energy at any given chemical potentials of O_2 and NO using the following equation [17]:

$$\Delta\gamma = \frac{G_{tot} - G_{stoich} - (1/2)n_O\mu_{O_2} - n_{NO}\mu_{NO}}{A},$$

where G_{tot}, G_{stoich} are the Gibbs energies of a slab of interest and a stoichiometric slab, respectively. n_0 and n_{NO} are the numbers of O and NO formula that a particular structure has compared with stoichiometric surface. μ_{O_2}, and μ_{NO} are the chemical potentials of gas phase O_2 and NO, respectively. The energy is normalized by surface area A. The Gibbs energy difference in the above equation can be related to DFT energy difference within the harmonic approximation for lattice vibrations as following [36]:

$$(G_{tot} - G_{stoich}) = (E_{tot} - E_{stoich}) + F^{vib}(T),$$
$$F^{vib}(T) = k_BT\sum_i \ln\left[2\sinh\left(\frac{h\nu_i}{2k_BT}\right)\right].$$

$F^{vib}(T)$ is the Helmholtz free energy due to adsorbate vibrations. ν_i are the computed vibrational modes of surface species, calculated assuming coverage independence and on a frozen, stoichiometric RuO_2 slabs. We neglect the relatively small PV and configurational entropy contributions to the Gibbs free energy.

By determining the configurations that minimize $\Delta\gamma$ as a function of μ_i, we construct the phase diagram shown in Fig. 5. At low O_2 potentials, adsorbed NO dominates the phase diagram, up to conditions at which NO adsorbs at both Ru_{cus} and O_{br} sites. At increasing oxygen potentials, adsorbed O_{cus} competes with adsorbed NO. Only at the highest oxygen potentials and intermediate NO potential does oxidized NO_x appear, in the form of NO_3 nitrate. In short, this picture shows that RuO_2 is much more effective in adsorbing NO than it is in converting to more highly oxidized species. Interestingly, NO^{**}_2 does not appear in the phase diagram, indicating that it is not thermodynamically stable against decomposition to adsorbed NO or oxidation to adsorbed NO_3. This picture again supports the assignment of observed surface-bound and oxidized NO species as adsorbed NO_3 [20].

To connect to laboratory conditions, the chemical potentials of O_2 and NO can be connected to ideal gas temperature and pressure using:

$$\mu = E_{DFT} + ZPE + H(T) - H(0\,K) + TS(T) + RT\ln\left(\frac{P}{P^\Theta}\right),$$

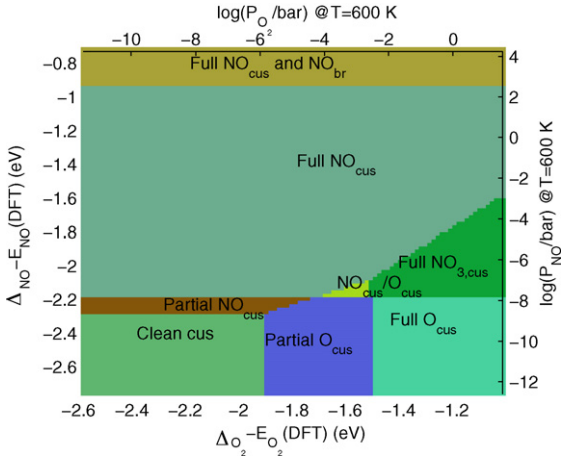

Fig. 5. Surface phase diagram of $NO_x + O_2$ on a stoichiometric RuO_2(1 1 0) surface. The corresponding gas pressures at $T = 600$ K are also shown. Except in the uppermost region, where NO adsorption at O_{br} becomes accessible, the labels indicate the most stable surface species at Ru_{cus} sites.

where $E_{DFT} + ZPE$ is the DFT calculated energy of gas phase O_2 or NO, $H(T)$ is the tabulated enthalpy [37], H(0 K) is the 0 K enthalpy extrapolated from available data, and P^Θ is the standard pressure, which we choose as 1 bar. Pressures shown in Fig. 5 correspond to 600 K. At ambient O_2 pressures and over a wide range of NO pressures, the stoichiometric RuO_2 surface is expected to be NO-saturated.

3.4. NO surface reactions

Given that NO dominates the RuO_2 surface chemistry, we next consider the kinetics of possible cus-bound NO surface reactions. We use the NEB method to identify minimum energy paths and reaction barriers for four relevant reactions (* refers to cus-bound species):

$$NO^* + O^* \rightarrow NO^{**}_2 \quad (2)$$

$$NO^* \rightarrow NO^* \quad \text{(diffusion)} \quad (3)$$

$$NO^* \rightarrow N^* + O^* \quad (4)$$

$$NO^* + N^* \rightarrow N_2O^* \quad (5)$$

The first reaction path is shown in Fig. 6a, ending at the NO_2 configuration shown in Fig. 3b. As noted above, this conversion is net endothermic, and the reaction pathway exhibits an additional barrier, so that the total forward activation energy is 1 eV. Along the reaction coordinate, the N atom from NO and the neighbor O_{cus} move towards each other, reducing the distance from an initial 3.17 Å to 1.66 Å at the product-like transition state (TS). The adjacent Ru_{cus} move closer as well, by 0.10 Å. At the TS, the ∠ONO is 110.8°, already very close to the 119.22° angle in the product state. NO oxidation is much less facile than is NO_2 decomposition on RuO_2, as has been observed in experiment [20]. For comparison, the corresponding conversion of CO* conversion to CO_2 is much more exothermic, has an earlier transition state, and has a barrier of 0.7 eV [10].

Fig. 6b shows the MEP for NO diffusion along a path in which the N center moves from one Ru_{cus} to the next. NO bridges two Ru_{cus} sites symmetrically at the transition state, with Ru–N distances elongated to 2.53 Å from 1.77 Å at the initial state (the calculated MEP lacks the symmetry of the actual path because of the combination of the climbing image algorithm and the use of an even number of beads. Nonetheless, the transition state itself is captured correctly). The calculated diffusion barrier along this path is about

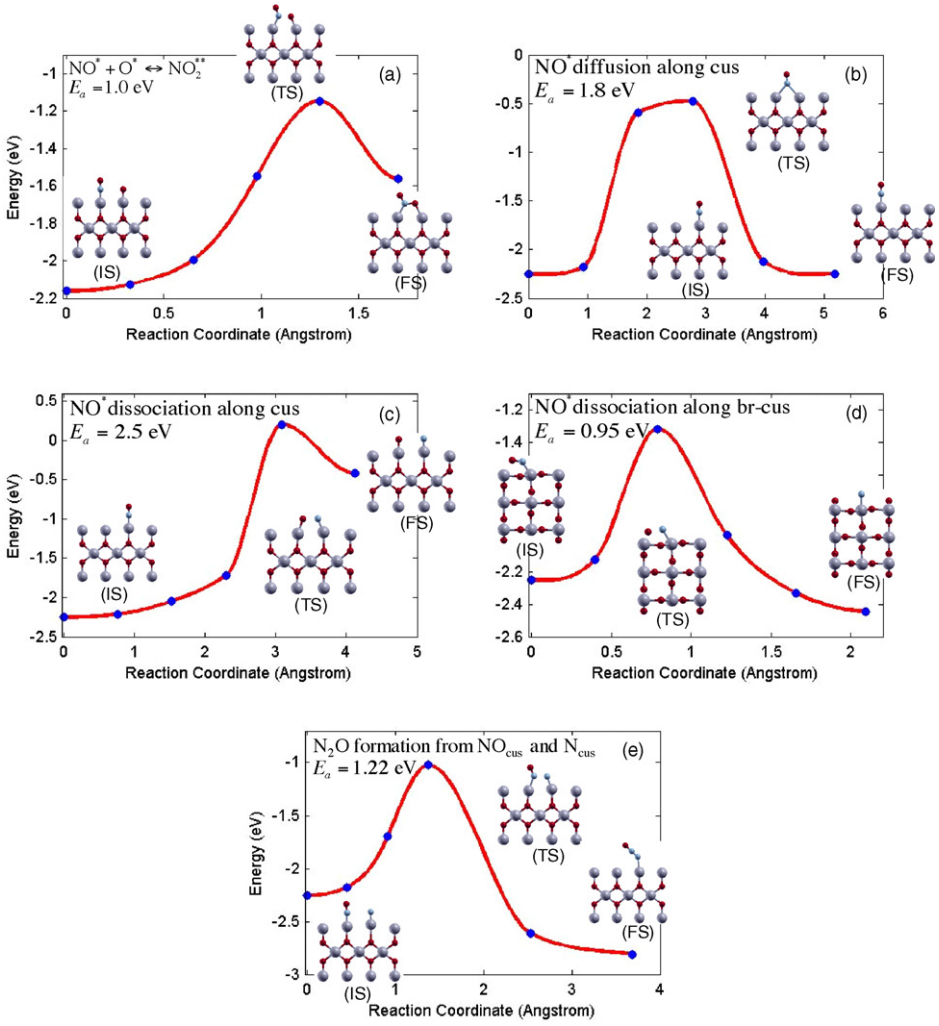

Fig. 6. Calculated MEPs for reactions of NO_{cus}, including initial (IS), transition (TS) and final states (FSs). The energies are plotted relative to gas phase NO_2 in (a) and relative to gas-phase NO otherwise. Molecular images are slices containing the planes of reaction.

1.8 eV, greater still than the 1.36 eV and 0.9 eV barriers for O and CO diffusion, respectively, along the cus row [27,38]. NO diffusion by this path is expected to be slow at moderate temperatures, and NO desorption likely competes effectively with surface diffusion processes.

A third potential reaction of adsorbed NO is dissociation to adsorbed N and O. Fig. 6c and d compare computed MEPs for dissociations across two cus sites and across adjacent cus and bridge sites, respectively. Cus–cus dissociation is 1.8 eV endothermic, reflecting the overall preference for Ru_{cus}–NO bonding over Ru_{cus}–N. Along the dissociation pathway, the NO molecule tilts and stretches until it is parallel to the cus row, bridging adjacent Ru_{cus}. The calculated barrier is 2.5 eV, ten times that for the analogous O_2 dissociation. This high barrier and large energy cost make the pathway to dissociate along cus rows practically impossible. The situation is much more favorable when considering dissociation into a bridge vacancy. Starting from the configuration shown in Fig. 2d, dissociation is slightly exothermic. Along the dissociation path, the O atom moves towards the br vacancy and the N towards to the Ru_{cus} as the N–O bond length increases to 1.67 Å at the TS. The computer barrier along this pathway is 0.95 eV.

N_2 has been observed to desorb after NO dosing and heating of an O–poor RuO_2(1 1 0) surface [18]. NO dissociation across br–cus may contribute to this N_2 production via recombinative desorption of adjacent N_{cus} atoms, as has been proposed to occur during NH_3 oxidation over RuO_2(1 1 0) [39]. We calculate N_{cus}–N_{cus} recombination to to be exothermic by −2.96 eV, with a modest desorption barrier of 0.8 eV (MEP not shown). Observed N_2O desorption may similarly have a contribution from N_{cus}, through combination with NO. Fig. 6e shows that along the MEP from NO* and N* to N_2O the two N atoms move towards one another, decreasing the N–N separation from 3.12 Å to 1.72 Å at the transition state. The NO fragment then lifts from Ru_{cus} and moves onto the adjacent N. The calculated barrier is a modest 1.22 eV and overall step exothermic −0.56 eV, or −2.81 eV relative to gas phase NO. In the presence of N*, such a path is a plausible route to N_2O. The computed adsorbed N–NO stretching frequency is calculated to be 291 meV, close to the experimental value of 283 meV [18]. The computed N_2O* desorption energy of 0.47 eV is also consistent with experimental observation [18]. N_{cus} may thus have a significant role in NO decomposition reactions over RuO_2(1 1 0).

4. Conclusions

We have used DFT supercell models to describe the adsorption and reaction chemistry of NO_x at the RuO_2(1 1 0) surface, a model transition metal oxide surface with well known catalytic properties. As is typical of NO_x [23], we find a rich adsorption chemistry involving both surface Ru and O centers. NO itself adsorbs strongly

at vacant Ru_{cus} sites. A thermodynamic analysis shows that over a wide range of O_2 and NO pressures, this cus-bound NO is the thermodynamically preferred surface species; under a limited window of conditions, cus-bound nitrate, NO_3, is stable. The latter can be conceived to arise from NO adsorption at an O_{cus}-saturated surface. The computed vibrational spectra of both of these NO_x surface states are consistent with experimental observation, and the latter provides an alternative assignment of the surface "NO_2" species that has recently been identified in recent experiments involving NO-dosing to O-covered RuO_2 [20].

NO_2 itself does not enjoy a window of stability, and in fact cus-bound NO_2 is unstable to decomposition to adsorbed O and NO. This conclusion is consistent with the observed thermal desorption of NO from an NO_2-dosed RuO_2(1 1 0) surface. The NO and O [22] binding energies show little coverage dependence, so that the coverage-driven mechanisms that promote catalytic NO oxidation to NO_2 over Pt metal [40] are inactive over this oxide. While RuO_2 is not expected to be active for NO oxidation, other oxides may strike a different balance between NO, O, and NO_2 binding energies that favor formation of the latter, as has been recently suggested for isostructural IrO_2(1 1 0) [21].

Again because of the high stability of adsorbed NO, NO dissociation is found to be facile only when dissociating into highly reactive bridge O vacancies. This dissociation route may contribute to the generation of N_2 and N_2O over reduced RuO_2 surfaces.

The results indicate that RuO_2 is much more effective at adsorbing NO than in oxidizing or decomposing it. In fact, this property could make RuO_2 useful as a reversible NO-storage material, in contrast to base metal oxides that only store NO_x in an oxidized form and require a secondary oxidation catalyst.

Acknowledgments

Financial support for this work was provided by the University of Notre Dame and the U.S. Department of Energy under grant DE-FG02-06ER15830. Some of figures are generated by XCrysDen [41].

References

[1] R.J. Farrauto, R.M. Heck, Catal. Today 55 (1–2) (2000) 179–187.
[2] W.F. Schneider, Fundamental Concepts in NO_x Catalysis Simulation, CRC Press, Boca Raton, 2005.
[3] S. Mulla, N. Chena, L. Cumaranatunge, G. Blau, D. Zemlyanov, W. Delgass, W. Epling, F. Ribeiroa, J. Catal. 241 (2006) 389.
[4] C.H. Kim, G. Qi, K. Dahlberg, W. Li, Science 327 (5973) (2010) 1624–1627.
[5] W.S. Epling, L.E. Campbell, A. Yezerets, N.W. Currier, J.E. Parks, Catal. Rev. 46 (2004) 163.
[6] C. Stampfl, M. Scheffler, Surf. Sci. 433 (1999) 119.
[7] H. Over, A.P. Seitsonen, E. Lundgren, M. Schmid, P. Varga, J. Am. Chem. Soc. 123 (2001) 11807.
[8] J. Wang, C. Fan, K. Jacobi, G. Ertl, Surf. Sci. 481 (2001) 113.
[9] J. Wang, C.Y. Fan, K. Jacobi, G. Ertl, J. Phys. Chem. B 106 (2002) 3422.
[10] S. Wendt, A.P. Seitsonen, H. Over, Catal. Today 85 (2003) 167.
[11] K. Reuter, M. Scheffler, Phys. Rev. Lett. 90 (2003) 046103.
[12] S.H. Kim, U.A. Paulus, Y. Wang, J. Wintterlin, K. Jacobi, G. Ertl, J. Chem. Phys. 119 (2003) 9729.
[13] M. Knapp, A.P. Seitsonen, Y.D. Kim, H. Over, J. Phys. Chem. B 108 (2004) 14392.
[14] K. Reuter, M. Scheffler, Phys. Rev. B 73 (2006) 045433.
[15] J. Assmann, V. Narkhede, N.A. Breuer, M. Muhler, A.P. Seitsonen, M. Knapp, D. Crihan, A. Farkas, G. Mellau, H. Over, J. Phys.: Condens. Matter 20 (2008) 184017.
[16] H. Wang, W.F. Schneider, Surf. Sci. 603 (2009) L91.
[17] H. Wang, W.F. Schneider, Phys. Chem. Chem. Phys. 12 (2010) 6367.
[18] Y. Wang, K. Jacobi, G. Ertl, J. Phys. Chem. B 107 (2003) 13918.
[19] S. Hong, T. Rahman, K. Jacobi, G. Ertl, J. Phys. Chem. C 111 (2007) 12361.
[20] K. Jacobi, Y. Wang, Surf. Sci. 603 (2009) 1600.
[21] H.-F. Wang, Y.-L. Guo, G. Lu, P. Hu, J. Phys. Chem. C 113 (2009) 18746.
[22] H. Wang, W.F. Schneider, J. Chem. Phys. 127 (2007) 064706.
[23] W.F. Schneider, J. Phys. Chem. B 108 (2004) 273.
[24] G. Kresse, J. Furthmüller, Comput. Mater. Sci. 6 (1996) 15.
[25] G. Kresse, J. Joubert, Phys. Rev. B 59 (1999) 1758.
[26] P.E. Blöchl, Phys. Rev. B 50 (1994) 17953.
[27] H. Wang, W.F. Schneider, D. Schmidt, J. Phys. Chem. C 113 (2009) 15266.
[28] G. Henkelman, B.P. Uberuaga, H. Jónsson, J. Chem. Phys. 113 (2000) 9901.
[29] G. Henkelman, H. Jónsson, J. Chem. Phys. 113 (2000) 9978.
[30] G. Mills, H. Jónsson, G.K. Schenter, Surf. Sci. 324 (1995) 305.
[31] H. Jónsson, G. Mills, K.W. Jacobsen, Nudged Elastic Band Method for Finding Minimum Energy Paths of Transitions, World Scientific, River Edge, NJ, 1998.
[32] R.F.W. Bader, Atoms in Molecules – A Quantum Theory, Oxford University Press, Oxford, 1990.
[33] G. Henkelman, A. Arnaldsson, H. Jónsson, Comput. Mater. Sci. 36 (2006) 354.
[34] K. Reuter, M. Scheffler, Phys. Rev. B 68 (2003) 045407.
[35] A.P. Seitsonen, D. Crihan, M. Knapp, A. Resta, E. Lundgren, J.N. Andersen, H. Over, Surf. Sci. 603 (2009) L113.
[36] M.V. Bollinger, K.W. Jacobsen, J.K. Nørskov, Phys. Rev. B 67 (2003) 085410.
[37] Y. Cengel, M. Boles, Thermodynamics, McGraw-Hill, 1998.
[38] S.H. Kim, J. Wintterlin, J. Phys. Chem. B 108 (2004) 14565.
[39] Y. Wang, K. Jacobi, W.D. Schone, G. Ertl, J. Phys. Chem. B 109 (2005) 7883.
[40] R.B. Getman, W.F. Schneider, ChemCatChem 2 (2010) 1450.
[41] A. Kokalj, Comput. Mater. Sci. 28 (2003) 155.